

1 Mapping yearly fine resolution global surface ozone
2 through the Bayesian Maximum Entropy data fusion
3 of observations and model output for 1990–2017

4 Marissa N. DeLang¹, Jacob S. Becker¹, Kai-Lan Chang^{2,3}, Marc L. Serre¹, Owen R. Cooper^{2,3},
5 Martin G. Schultz⁴, Sabine Schröder⁴, Xiao Lu⁵, Lin Zhang⁵, Makoto Deushi⁶, Beatrice Josse⁷,
6 Christoph A. Keller^{8,9}, Jean-François Lamarque¹⁰, Meiyun Lin^{11,12}, Junhua Liu^{8,9}, Virginie
7 Marécal⁷, Sarah A. Strode^{8,9}, Kengo Sudo^{13,14}, Simone Tilmes¹⁰, Li Zhang^{11,12,15}, Stephanie E.
8 Cleland¹, Elyssa L. Collins¹, Michael Brauer^{16,17}, J. Jason West^{*,1}

9 ¹Department of Environmental Sciences and Engineering, University of North Carolina at Chapel Hill, Chapel Hill,
10 NC, USA

11 ²Cooperative Institute for Research in Environmental Sciences, University of Colorado, Boulder, CO, USA

12 ³NOAA Chemical Sciences Laboratory, Boulder, CO, USA

13 ⁴Jülich Supercomputing Centre (JSC), Forschungszentrum Jülich, Jülich, Germany

14 ⁵Laboratory for Climate and Ocean-Atmosphere Studies, Department of Atmospheric and Oceanic Sciences, School
15 of Physics, Peking University, Beijing, China

16 ⁶Meteorological Research Institute (MRI), Tsukuba, Japan

17 ⁷Centre National de Recherches Météorologiques, Université de Toulouse, Météo-France, CNRS, Toulouse, France

18 ⁸NASA Goddard Space Flight Center, Greenbelt, MD, USA

19 ⁹Universities Space Research Association, Columbia, MD, USA

20 ¹⁰National Center for Atmospheric Research, Boulder, CO, USA

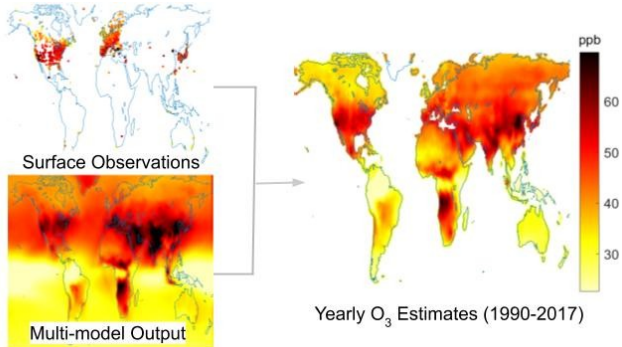
21 ¹¹NOAA Geophysical Fluid Dynamics Laboratory, Princeton, NJ, USA

22 ¹²Program in Atmospheric and Oceanic Sciences, Princeton University, Princeton, NJ, USA

23 ¹³Graduate School of Environmental Studies, Nagoya University, Nagoya, Japan

- 24 ¹⁴Japan Agency for Marine-Earth Science and Technology (JAMSTEC), Yokosuka, Japan
- 25 ¹⁵Department of Meteorology and Atmospheric Science, Pennsylvania State University, University Park, PA. USA
- 26 ¹⁶Institute for Health Metrics and Evaluation, University of Washington, Seattle, Washington, USA
- 27 ¹⁷School of Population and Public Health, University of British Columbia, Vancouver, British Columbia, Canada

28 TOC GRAPHIC



29

30 ABSTRACT

31 Estimates of ground-level ozone concentrations are necessary to determine the human
32 health burden of ozone. To support the Global Burden of Disease Study, we produce yearly fine
33 resolution global surface ozone estimates from 1990 to 2017 through a data fusion of
34 observations and models. As ozone observations are sparse in many populated regions, we use a
35 novel combination of the M³Fusion and Bayesian Maximum Entropy (BME) methods. With
36 M³Fusion, we create a multi-model composite by bias-correcting and weighting nine global
37 atmospheric chemistry models based on their ability to predict observations (8,834 sites globally)
38 in each region and year. BME is then used to integrate observations, such that estimates match
39 observations at each monitoring site with the observational influence decreasing smoothly across
40 space and time until the output matches the multi-model composite. After estimating at 0.5°
41 resolution using BME, we add fine spatial detail from an additional model, yielding estimates at
42 0.1° resolution. Observed ozone is predicted more accurately ($R^2=0.81$ at test point, 0.63 at 0.1°,
43 0.62 at 0.5°) than the multi-model mean ($R^2=0.28$ at 0.5°). Global ozone exposure is estimated to
44 be increasing, driven by highly populated regions of Asia and Africa, despite decreases in the
45 United States and Russia.

46

47 INTRODUCTION

48 Tropospheric ozone is harmful to human health through respiratory health effects
49 associated with short and long term exposure.¹⁻³ Additionally, tropospheric ozone influences
50 climate³ and damages plant growth.^{5,6} Surface ozone estimates at fine spatial resolution, which
51 are required to determine the human health burden of ozone exposure, are typically based on two
52 sources: monitoring networks and atmospheric chemistry models. Monitoring networks provide
53 high spatial coverage of surface ozone observations in North America, Europe, Japan, South
54 Korea, and recently China; however, stations are scarce elsewhere.⁷ Global atmospheric models
55 provide concentration estimates across many years and cover all world regions; however, models
56 have biases.⁸

57 The Global Burden of Disease (GBD) Study conducts a comparative risk assessment that
58 estimates the health burden caused by specific risk factors from 1990 to present day, updated
59 regularly. Two ambient air pollution risk factors are analyzed: fine particulate matter (PM_{2.5}) and
60 ozone.^{9,10} GBD PM_{2.5} estimates are generated through a combination of satellite retrievals and
61 land use information with a single atmospheric model calibrated to surface observations with a
62 Bayesian hierarchical model.^{11,12} In contrast, global ozone estimates prior to GBD 2017¹³ were
63 provided by a single model with no bias correction to observations.¹⁴ Satellite measurements
64 provide PM_{2.5} estimates at fine resolution, but do not accurately detect surface ozone.^{14,15}

65 The recent Tropospheric Ozone Assessment Report (TOAR) collected ozone
66 observations from thousands of sites around the world, which made it possible to incorporate
67 surface observations into GBD estimates.^{7,16} For GBD 2017, TOAR observations were combined
68 with six atmospheric models from phase one of the Chemistry-Climate Model Initiative
69 (CCMI)¹⁷ using the M³Fusion method for the average of 2008 to 2014.¹⁸ In M³Fusion, the models

70 were bias corrected and combined by finding the optimal linear combination of models in each
71 world region, weighted based on their performance with respect to observations. Within two
72 degrees of a monitoring station, the multi-model composite was then replaced with a spatial
73 interpolation of observations. The 2008–2014 ozone distribution was extended backwards
74 (1990–2008) by scaling with cubic splines relative to prior GBD ozone estimates and forwards
75 (2014–2017) by extending the annual rate of change from 2012, for use in GBD 2017.¹³

76 While the M³Fusion method significantly improved upon previous GBD ozone estimates,
77 we identify a potential for further improvements. In particular, the correction within two degrees
78 of an observation can create discontinuities, which could be improved by using advanced
79 geostatistical techniques that combine model output with observations using smooth weighting
80 across space. Here we use a novel combination of the M³Fusion and Bayesian Maximum
81 Entropy (BME) methods,¹⁹⁻²² which is uniquely suited to the challenges of mapping global ozone
82 concentrations, as only observations and models provide useful information and observations are
83 sparse in some world regions. The regional “large-scale” bias correction and weighting of
84 models in the M³Fusion multi-model composite provides the best estimate of ozone far from
85 observations. Then BME provides a local “small-scale” correction, by smoothly integrating
86 observations in both space and time such that estimates match observations at the measurement
87 site, and the influence of those observations decreases with distance according to the
88 spatiotemporal covariance. Since ozone monitoring is inconsistent, allowing observations to
89 affect predictions across time could provide more accurate estimates. Near observation locations,
90 therefore, ozone estimates will be strongly influenced by observations. BME has previously
91 been used to fuse ozone observations with models on state and national scales,²³⁻²⁵ but it has not
92 been used previously globally, and apart from Chang et al.,¹⁸ we are not aware of any global data

93 fusion of ozone observations and models.

94 We aim to estimate global fine resolution (0.1°) surface ozone for each year from 1990 to
95 2017 to support the GBD 2019 Study by combining surface observations with multiple global
96 atmospheric models by first using M³Fusion to create multi-model composites, and then applying
97 BME to smoothly fuse multi-model composites with observations in space and time. We
98 improve upon the single 7-year mean ozone fields produced for GBD 2017¹⁸ by producing yearly
99 output for 1990-2017, including additional observations and model output, smoothly weighting
100 observations across space and time, and applying fine spatial structure based on fine resolution
101 model output. To add fine spatial resolution for GBD, we apply the fine-scale spatial patterns
102 from a global fine resolution model simulation.²⁶ Our annual global ozone maps were used by
103 GBD 2019, which extrapolated to 2019 and estimated 365,000 (95% CI: 175,000-564,000)
104 premature chronic obstructive pulmonary disease deaths globally, or 6.21 (2.99-9.63) million
105 disability adjusted life years, from ambient ozone exposure in 2019.²⁷

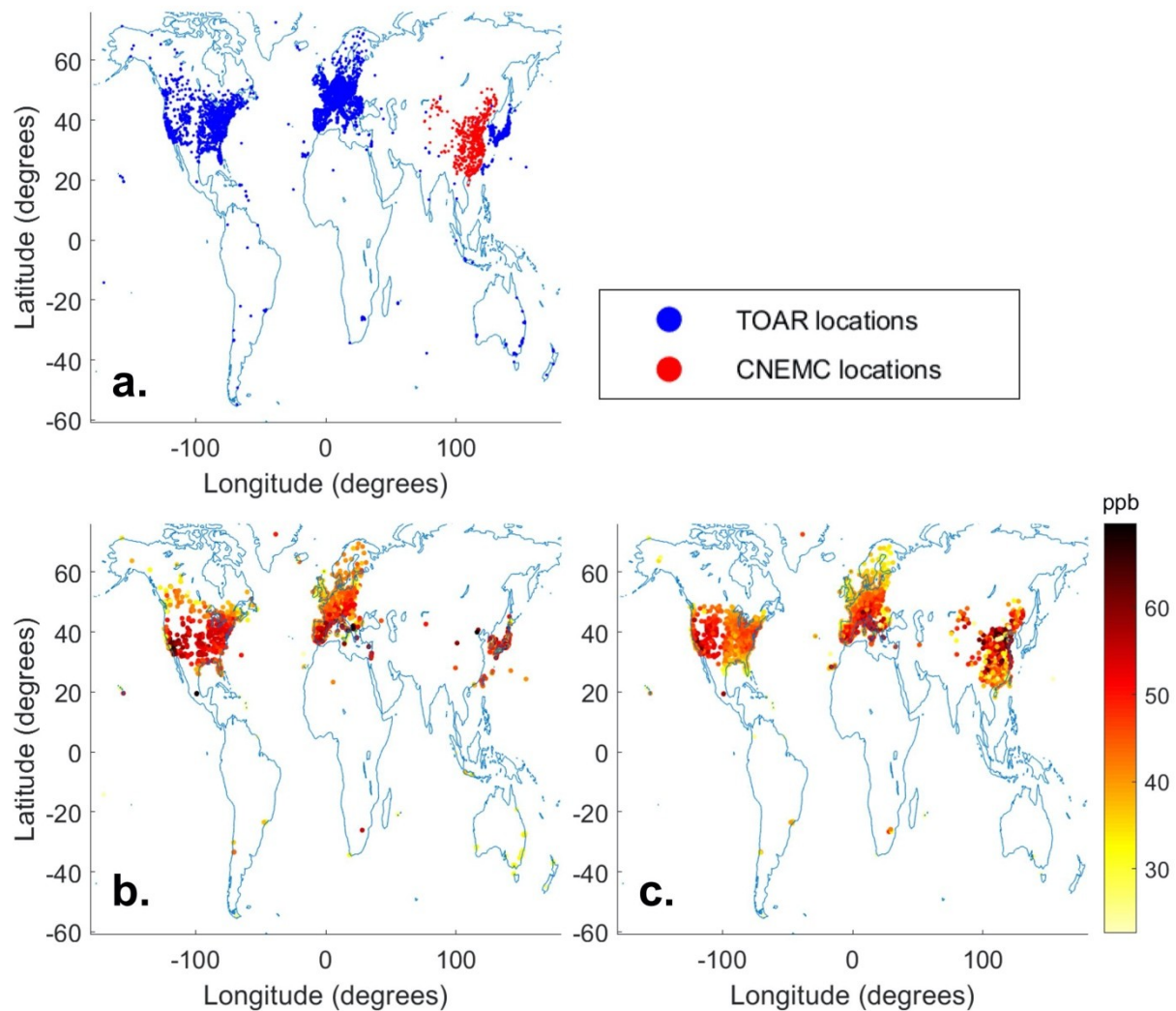
106 MATERIALS AND METHODS

107 M³Fusion and BME are used in sequence to estimate global surface ozone concentrations.
108 Other methods have been applied on smaller scales, such as neural networks using
109 meteorological and emission variables to predict ozone,^{28,29} but those relationships may not apply
110 elsewhere, and those methods are inappropriate where there are no observations.

111 GBD's ozone metric for quantifying health outcomes from long term ozone exposure is
112 the ozone season daily maximum 8-hour mixing ratio (OSDMA8).² OSDMA8 is calculated as
113 the annual maximum of the six-month running mean of the monthly average daily maximum 8-
114 hour mixing ratio, including months through March of the following year to contain the Southern
115 Hemisphere summer. All observations, model output, and estimates are reported here as

116 OSDMA8.

117 ***Surface Ozone Observations.*** We include surface ozone observations from TOAR and the
118 Chinese National Environmental Monitoring Center (CNEMC) Network (Figure 1). TOAR is the
119 world's largest collection of in-situ hourly surface ozone observations covering 1970-2015.^{16,30}
120 The database contains dense observations in North America, Europe, Japan, and South Korea,
121 and sparse observations elsewhere.⁷ The database was updated for this project to include readily-
122 available datasets for the years 2015–2017, but measurements were not updated for all nations
123 previously included. CNEMC includes surface ozone observations for 2013–2017 in China,³¹
124 which were quality-controlled using the same algorithm that TOAR applies elsewhere. The total
125 observations ranged from a minimum of 1,199 in 1990 to a maximum of 4,999 in 2015. The
126 incomplete TOAR update in 2016 and 2017 yielded fewer observation sites than 2015.



127

128 **Figure 1.** (a) TOAR and CNEMC monitoring locations with at least one valid yearly OSDMA8
 129 observation over 1990–2017. In total, there are 8,834 monitoring stations, 7,269 from TOAR and
 130 1,565 from CNEMC. (b) Surface observations as OSDMA8 in 2005, with an average of 45.5 ppb
 131 and maximum of 82.2 ppb in Mexico City, Mexico. (c) Surface observations as OSDMA8 in
 132 2015, with an average of 46.2 ppb and maximum of 80.9 ppb in Zibo, China.

133 **Atmospheric Chemistry Model Simulations.** We incorporate modeled ozone from nine
 134 atmospheric chemistry model simulations (Table 1). The models, mostly from CCMI,¹⁷ report
 135 output for 1990–2010 from the specified dynamics REF-C1SD experiment,^{17,32} which uses

136 annual MACCity emissions .^{33,34} Three models, MOCAGE, MERRA2-GMI, and GFDL-AM3,
 137 were extended past 2010. To increase models after 2010, we include output from the specified
 138 dynamics experiments of MRI-ESM2.0 and GFDL-AM4, for modified Coupled Model
 139 Intercomparison Project Phase 6 (CMIP6)³⁵ experiments. Hourly ozone mixing ratios were
 140 processed to OSDMA8, using the same algorithm as for observations.

141 **Table 1.** Nine atmospheric chemistry models used in this study.

Model	Years	Resolution	Experiment	Reference
CESM1 CAM4-Chem	1990–2010	1.9° × 2.5°	CCMI REF-C1SD	36
CESM1 WACCM	1990–2010	1.9° × 2.5°	CCMI REF-C1SD	37,38
CHASER	1990–2010	2.8° × 2.8°	CCMI REF-C1SD	39-41
GFDL AM3	1990–2014	2° × 2.5°	CCMI REF-C1SD	42-44
GFDL AM4	2010–2016	1° × 1.25°	CMIP6 nudged to NCEP winds ^a	45,46
MERRA2-GMI	1990–2017	0.5° × 0.625°	MACCity and GFED-4s emissions ^b	47,48
MOCAGE	1990–2016	2° × 2°	CCMI REF-C1SD	49,50
MRI-ESM1r1	1990–2010	2.8° × 2.8°	CCMI REF-C1SD	51
MRI-ESM2.0	2011–2017	2.8° × 2.8°	CMIP6 historical and ssp370 ^c	452

142 ^a Nudged to observed meteorology similar to GFDL-AM3 and uses anthropogenic emissions modified from CMIP6

143 to reflect recent NO_x trends in China and the United States⁴⁵

144 ^b MACCity anthropogenic emissions with biomass burning emissions from Global Fire Emissions Dataset version

145 4s^{47,48}

146 ^c Emissions from the CMIP6 historical (2011–2014) and ssp370 (2015–2017) experiments⁵²

147 **Multi-model Composite.** We use M³Fusion to create multi-model composites of the models
 148 available in each year from 1990–2017.¹⁸ This method corrects for model bias and finds the
 149 linear combination of models in each region and year that minimizes the mean square error as
 150 compared to observations. Since model resolution varies, we use bilinear interpolation to smooth
 151 yearly OSDMA8 to a 0.5° × 0.5° grid. We interpolate yearly observations from irregular
 152 monitoring station locations to the 0.5° grid using the stochastic partial differential equation
 153 approach.⁵³ In each of eight geographical regions (Figure S1) and each year, we weight each

154 model to minimize the difference between the multi-model average and spatially interpolated
155 observations based on a constrained least squares approach:

$$156 \quad \underset{\{\alpha_r, \beta_{rk}; k=1, \dots, n\}}{\text{minimize}} \sum_{s_g \in \text{Region } r} \left(\hat{y}(s_g) - \alpha_r - \sum_{k=1}^n \beta_{rk} \eta_k(s_g) \right)^2, \quad (1)$$

$$157 \quad \text{subject to } \sum_{k=1}^n \beta_{rk} = 1 \wedge \beta_{rk} \geq 0$$

158 where s_g is the grid cell at 0.5° resolution, $\hat{y}(s_g)$ is the spatially interpolated observations, $\{\eta_k(s_g);$

159 $k=1, \dots, n\}$ is the model output on the same grid from the n models available, α_r is a constant that

160 corrects overall bias in each region, and β_{rk} is an optimal weight for the k -th model in region r .

161 All model weights are constrained to be positive and sum to 1. The constant offset α_r guarantees

162 that the residuals from this optimization have a zero mean, through which the mean model bias is

163 corrected in each region.¹⁸

164 Since M³Fusion relies on spatially interpolated observations to determine model weights,

165 we modify the method for data sparse regions and years. In North America and Europe, we use

166 weights based on each individual year's models and observation values. For all other regions, we

167 calculate individual year weights for 2000–2010, and apply weights from the aggregated 2000–

168 2010 period to 1990–1999. For 2011–2017, East Asia uses individual year weights, while South

169 America, Africa, South-Central Asia, Russia, and Oceania use weights from the aggregated

170 2011–2014 period, for which the TOAR dataset was complete.

171 **Bayesian Maximum Entropy Methodology.** BME is a geostatistical method that incorporates

172 multiple forms of knowledge to predict an estimate of a homogenous, stationary, space-time

173 random field.^{19–22} Using BME, we combine surface observations and annual multi-model

174 composites to calculate an ozone estimate that matches observations at each monitoring station

175 and the observational influence gradually diminishes across space and time until it matches the
 176 multi-model composite. BME has been described previously, including in the fusion of ozone
 177 observations with model output at state and national scales^{120-24,54}. We model the offset-
 178 removed, homogeneous space-time random field (S/TRF) $X(\mathbf{p})$ at the space-time coordinate
 179 $\mathbf{p}=(s,t)$.²⁴ In BME, there are two forms of knowledge: site-specific and general. Site-specific
 180 knowledge can consist of hard data, with no assumed uncertainty, and soft, probabilistic data.
 181 Here we only have hard data, which is the linear limiting case of the BME data integration
 182 framework.²⁴ We remove the offset, the multi-model composite at monitoring stations ($o_z(\mathbf{p}_0)$),
 183 from OSDMA8 observations (z_0) at monitoring station locations \mathbf{p}_0 to obtain hard data \mathbf{x}_0 :

$$184 \quad \mathbf{x}_0 = z_0 - o_z(\mathbf{p}_0) \quad (2)$$

185 The general knowledge base of $X(\mathbf{p})$ includes the mean function $m_x(\mathbf{p}) = E[X]$, which is assumed
 186 to be zero, and the covariance function $c_x(\mathbf{p}, \mathbf{p}') = E[(X(\mathbf{p}) - m(\mathbf{p}))(X(\mathbf{p}') - m(\mathbf{p}'))]$, which is determined
 187 by the experimental covariance of \mathbf{x}_0 :

$$188 \quad \hat{c}_x(r, \tau) \approx \frac{1}{N(r, \tau)} \sum_{i=1}^{N(r, \tau)} x_{head,i} x_{tail,i} - m_x^2 \quad (3)$$

189 where $N(r, \tau)$ is the number of pairs of points with values (x_{head}, x_{tail}) separated by a distance r and
 190 time τ , and m_x is the mean of \mathbf{x}_0 . For the S/TRF $X(\mathbf{p})$, we use an exponential covariance model to
 191 best fit the experimental covariance:

$$192 \quad c_x(r, \tau) = C \left[\gamma \exp \frac{-3r}{a_{r1}} \exp \frac{-3\tau}{a_{t1}} + \lambda \exp \frac{-3r}{a_{r2}} \exp \frac{-3\tau}{a_{t2}} + (1 - \gamma - \lambda) \exp \frac{-3r}{a_{r3}} \exp \frac{-3\tau}{a_{t3}} \right] \quad (4)$$

193 with parameters in the supporting information. The BME estimation process involves using

194 general knowledge to obtain the maximum entropy prior probability density function (PDF) of
195 f_G , updating f_G by integrating site-specific knowledge to obtain the epistemic Bayesian posterior
196 PDF f_K , which provides a complete stochastic description of $X_k=X(\mathbf{p}_k)$ at the estimation point \mathbf{p}_k ,
197 and computing space-time estimates based on f_K . The posterior PDF is defined as:

$$198 \quad f_K(x_k) = \left(\frac{f_G(x_0, x_k)}{f_G(x_0)} \right) \quad (5)$$

199 where x_k is the offset-removed estimate at points \mathbf{p}_k . We define the ozone space-time random
200 field (S/TRF), $Z(\mathbf{p})$, as the sum of $X(\mathbf{p})$ and the offset (multi-model composite):

$$201 \quad Z(\mathbf{p}) = X(\mathbf{p}) + o_z(\mathbf{p}) \quad (6)$$

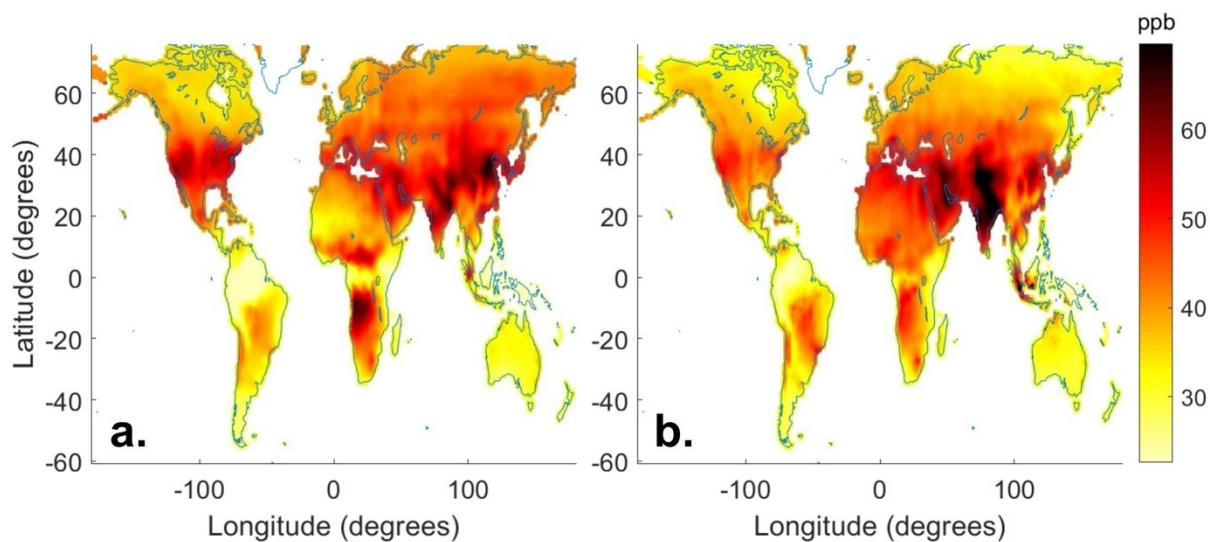
202 We obtain the estimated OSDMA8 z_k at \mathbf{p}_k by obtaining the BME estimate x_k for the S/TRF $X(\mathbf{p})$
203 at \mathbf{p}_k , and adding back $o_z(\mathbf{p}_k)$.

204 ***Fine Resolution Addition.*** We calculate ozone BME estimates at 0.5° resolution; however, a
205 finer resolution is desirable for GBD to reduce spatial misalignment with population. Since
206 neither the observations nor the models represent ozone at fine resolution, except where
207 observations are dense, we use the spatial distribution of a fine resolution model. We use output
208 from a NASA G5NR-Chem model²⁶ simulation from July 2013 to June 2014 at 0.125°
209 resolution, which we regrid to 0.1° resolution, to provide the fine spatial structure within each
210 0.5° grid cell for each year 1990-2017. While we do not expect the modeled 2013–2014 ozone to
211 be accurate for every year, we use the modeled spatial distribution to inform the fine-scale spatial
212 pattern for each year, assuming the fine spatial patterns do not change. We calculate the
213 difference between the BME estimate and the average of NASA G5NR-Chem grid cells for each

214 0.5° grid cell, and add this difference to each NASA G5NR-Chem grid cell at 0.1° to obtain our
215 BME estimate at 0.1°. Consequently, the sub-grid variability of the output matches the G5NR-
216 Chem model, and the average of each 0.5° grid cell remains the same as the BME estimate
217 (Figures S2-3).

218 RESULTS

219 **Multi-model Composite.** We determine weights for each model in each region and year (Table
220 S1). In most regions and years, the multi-model mean ozone (the simple average of all models) is
221 biased high, as models generally overpredict ozone.^{8,18} Therefore, the M³Fusion multi-model
222 composite (Figure 2) tends to decrease average ozone compared to the multi-model mean.

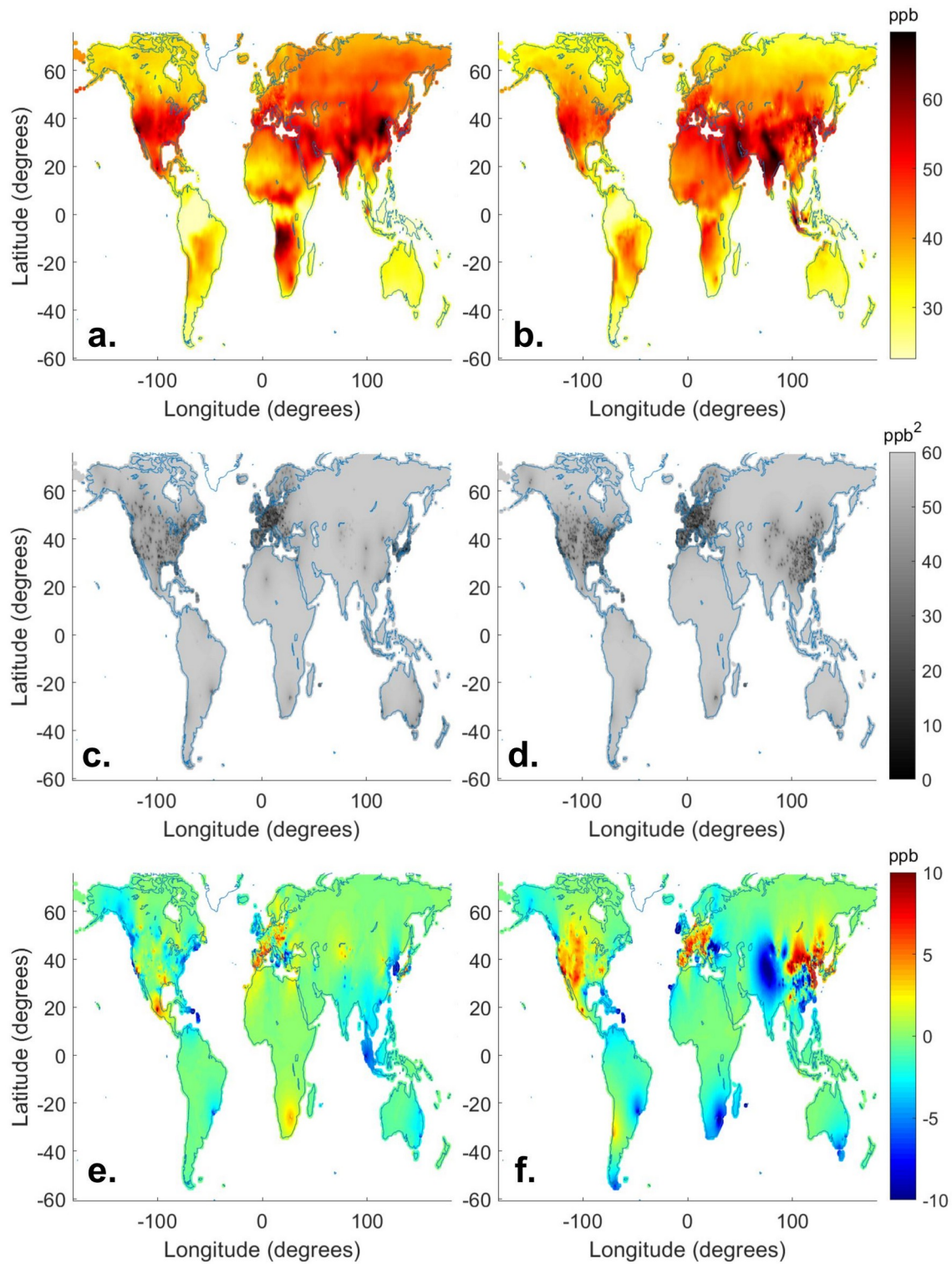


223

224 **Figure 2.** Multi-model composite as OSDMA8 in 2005 (a) and 2015 (b).

225 **BME Coarse Resolution Output.** We obtain yearly ozone output at 0.5° resolution, with an
226 associated variance at each estimation point (Figure 3; Figures S4-31). The ozone output matches
227 an observation at its space-time location, and the observation's influence decreases in space and
228 time according to the derived spatiotemporal covariance (Equation S3). In regions with high
229 observational coverage, there is greater spatial variation in our output, whereas less monitored

230 regions are smoother. Across the years, areas of low estimated ozone include the Amazon,
231 Oceania, and southeastern Africa; while high ozone is estimated in East Asia, South-Central
232 Asia, western North America, and central Africa. The Amazon and central Africa are
233 unmonitored; therefore, their respective low and high ozone estimates are based on model output
234 reflecting ozone chemical destruction over the Amazon⁵⁵ and biomass burning in Africa.⁵⁶
235 In BME, observations are treated as hard data with no variance; therefore, regions with the
236 highest number of observations have the lowest variance, such as North America, Europe, and
237 Japan in 2005 and additionally eastern China in 2015. Away from observations, the output is
238 equal to the multi-model composite and the variance reaches a maximum of 60 ppb², equal to the
239 variance of the offset removed observations. To visualize how BME adjusted the multi-model
240 composite using observations, we subtract the multi-model composite from our BME estimate
241 (Figure 3). In unmonitored regions, there is no difference between our BME output and the
242 multi-model composite. When adding fine resolution in the final step, differences on the global
243 scale are unnoticeable (Figures S4-31).



244

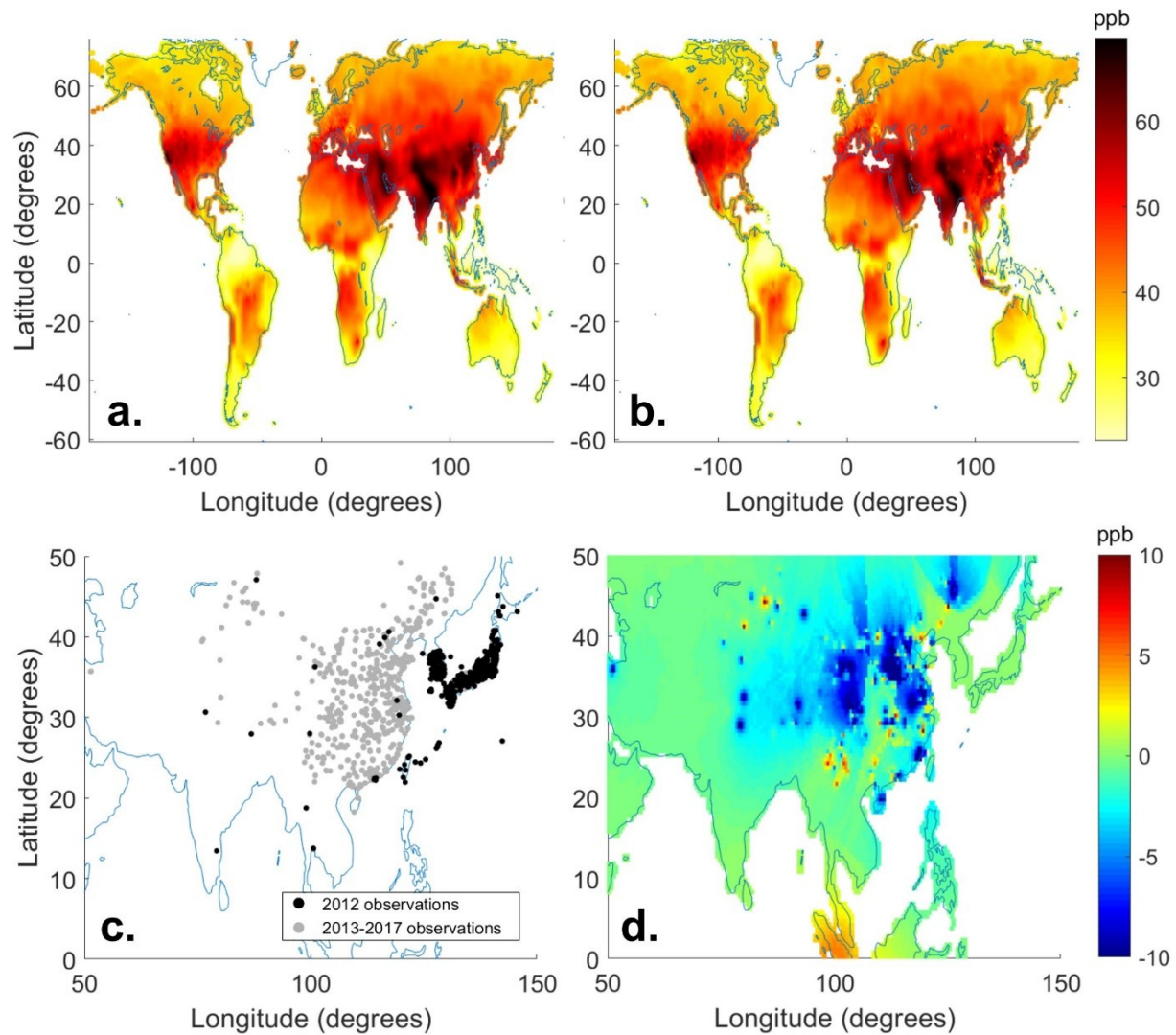
245 **Figure 3.** BME estimate as OSDMA8 for 2005 (a) and 2015 (b). BME variance for 2005 (c) and

246 2015 (d). Effect of BME fusion of observations (BME estimate minus multi-model composite)

247 for 2005 (e) and 2015 (f). Positive values occur where our estimate is higher than the multi-
248 model composite, negative values where our estimate is lower.

249 ***Influence of Observations through Time.*** The ability of an observation to influence other years
250 is an important component of our method, since observational coverage changes, generally with
251 more stations being added. The extent of an observation’s influence on other years depends on
252 the number of nearby stations in space and time, with more remote stations having a longer
253 temporal influence. In addition to the space-time BME estimates above, we also perform “space-
254 only” BME, in which observations only influence ozone estimates across space in a single year.

255 By taking the difference between space-time and space-only results, we evaluate how
256 observations influence other years. Since the CNEMC observations started in 2013, analyzing
257 2012 highlights their temporal influence (Figure 4). On the global scale, the differences between
258 the space-time and space-only methods are difficult to distinguish, but the major differences
259 occur across China. Most of the non-zero differences occur in areas where CNEMC observations
260 were added in 2013–2017, showing the influences of those observations (Figure 4). Whereas
261 Figure 4 shows that BME largely decreased ozone estimates over China in 2012, the effect of
262 adding BME differed among years, including increasing ozone in 2015 and 2016 (Figures S29-
263 30).



264

265 **Figure 4.** (a) Space-only BME result in 2012 as OSDMA8. (b) Space-time BME result in 2012
 266 as OSDMA8. (c) Observation locations in 2012 and 2013–2017. (d) Effect of BME space-time
 267 influence of observations (space-time BME minus the space-only BME) for 2012.

268 **Evaluation.** To evaluate our results, we perform a leave one out cross validation (LOOCV),
 269 where one observation is removed and we evaluate our ability to predict this observation, in five
 270 scenarios:

- 271 - Multi-model mean: average of all model output available in a given year.
- 272 - Multi-model composite: combination of model output using M³Fusion.

- 273 - Space-only correction: BME corrected multi-model composite where observations
- 274 only influence across space in a single year.
- 275 - Space-time correction: BME corrected multi-model composite where observations
- 276 influence across space and time.
- 277 - Fine resolution: space-time corrected output with fine resolution from the NASA
- 278 G5NR-Chem model.

279 LOOCV was performed using two methods: predicting ozone at the test point’s grid cell and at
 280 the test point’s specific space-time location. The grid cell prediction was performed to allow a
 281 fair comparison between scenarios, since the fine resolution addition is limited to predicting at
 282 the grid cell level, and to evaluate the benefit of increasing output resolution. When predicting at
 283 the test point’s grid cell, each subsequent scenario improved performance, as shown by the root
 284 mean square error (RMSE) (Table 2). The multi-model composite outperforms the multi-model
 285 mean across all validation statistics. Correcting the multi-model composite across space using
 286 observations improves the results, which is further amplified by correcting across both space and
 287 time. Adding fine spatial structure, which gives our final output, slightly improves performance
 288 relative to the space-time scenario. All methods overestimate ozone in comparison to
 289 observations, as shown by the mean error (Table 2), though our final product is biased high only
 290 slightly.

291 **Table 2.** LOOCV statistics,^a where results are evaluated in the 0.5 or 0.1 grid cells containing the
 292 test point, or at the test point’s space-time location.

293

Scenario	Prediction location	RMSE	ME	R ²	varE	varZ
		(ppb)	(ppb)		(ppb ²)	(ppb ²)

Multi-model Mean	0.5° grid cell	13.76	11.00	0.28	68.48	62.08
Multi-model Composite	0.5° grid cell	7.82	1.05	0.30	60.03	43.09
Space-only Correction	0.5° grid cell	6.01	0.42	0.57	36.00	60.14
Space-time Correction	0.5° grid cell	5.62	0.57	0.62	31.30	62.01
Fine Resolution	0.1° grid cell	5.54	0.22	0.63	30.68	63.24
Multi-model Composite	Test point's location	7.82	1.07	0.30	60.00	43.19
Space-time Correction	Test point's location	3.99	0.01	0.81	15.94	81.26

294 ^a Root mean square error (RMSE), mean error (ME), R-squared (R^2), variance of error (varE), and variance of the
295 estimated ozone (varZ). The mean and variance of observed ozone are $mO=45.62$ ppb and $varO=81.96$ ppb²,
296 respectively. Statistic definitions are included in Table S2.

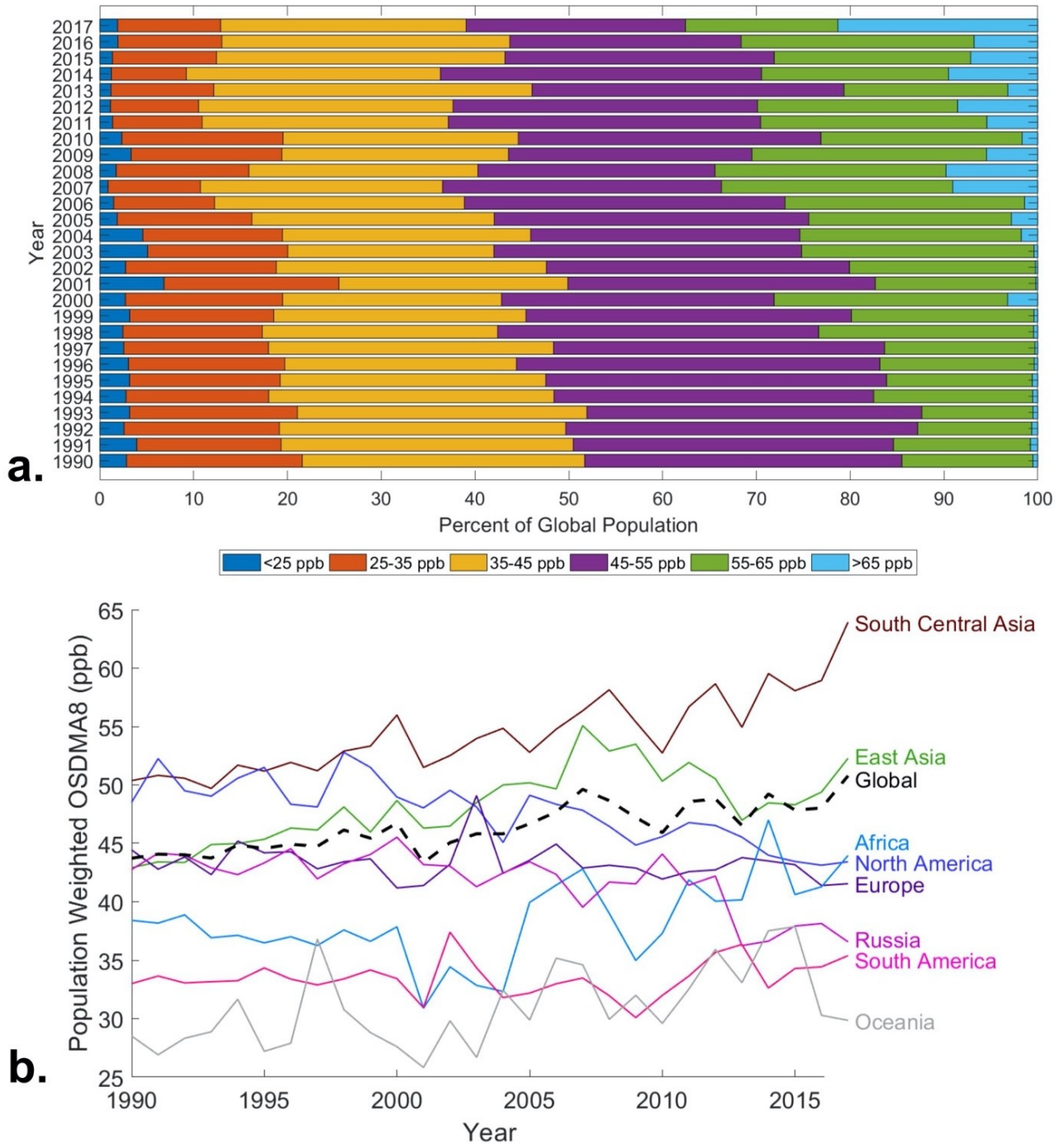
297

298 For comparison with other studies, we include statistics for predicting at the specific
299 space-time location (Table 2). The addition of the space-time correction to the multi-model
300 composite decreased RMSE from 7.82 to 3.99 ppb, a 49% reduction. In comparison, for Chang
301 et al.¹⁸, the correction to the multi-model composite decreased the RMSE from 5.16 to 3.82 ppb,
302 a 26% reduction. The greater relative reduction in RMSE here is attributed to the incorporation
303 of both spatial and temporal autocorrelation, and shows our improvement to Chang et al.¹⁸.

304 ***Population-Weighted Ozone Trends.*** With our yearly output, we use global gridded population
305 from GBD 2019 to analyze trends in population-weighted ozone as an indicator of exposure. The
306 2019 global population is used for all years, meaning that differences in exposure result from
307 changes in ozone, not population. To determine how ozone exposure has changed from 1990–
308 2017, we examine the percent of the global population exposed to intervals of OSDMA8 (Figure
309 5). Global ozone exposure increases over this period, with an increase in the global population
310 exposed to highest concentrations (>55 ppb). In 2017, 21.3% of the global population was
311 exposed to OSDMA8 higher than 65 ppb, more than double the percentage in any previous year.
312 Note that the OSDMA8 metric is not compared easily with national standards or WHO

313 guidelines, which are typically based on the daily 8-hr maximum. For perspective, the risk of all-
314 cause, circulatory, and respiratory mortality reportedly increases by 2%, 3%, and 12% per 10 ppb
315 increase in long-term OSDMA8, respectively, with some evidence that ozone influences
316 mortality at concentrations above about 35 ppb.²

317 We analyze the population-weighted trends from 1990–2017 for each world region
318 (Figure 5) and the most populous countries (Figure S32). Globally, there is a positive trend in
319 population weighted ozone for 1990–2017, driven in large part by positive trends in highly
320 populated and polluted regions of South-Central Asia, East Asia, and Africa. Low population-
321 weighted ozone occurs in South America and Oceania. Negative trends occur in North America
322 and Russia; Europe has a weak negative trend, with the European Union showing no change.
323 We caution that these trends are most uncertain before 2000 and in regions with few
324 observations; under these conditions our estimated trends mainly reflect models and a small
325 number of observations. Year-to-year changes in ozone in regions with few observations may
326 also result from using different model weights in individual years. These trends are supported by
327 a previous analysis of TOAR data for 2000–2014 summertime ozone, which found a positive
328 trend in East Asia and negative trends in North America and Europe.⁵⁷ Similarly, a study of
329 CNEMC observations showed increases in China for 2013–2017.³¹ One study suggests that the
330 2013-2017 increase over China was influenced most by the decrease of PM_{2.5}, which increased
331 HO_x radicals⁵⁸; therefore, a PM_{2.5} increase might explain our estimated 2007-2013 ozone
332 decrease. Increasing trends in other regions with few observations, including Africa and South
333 Central Asia are supported by long-term aircraft⁵⁹ and satellite column observations.⁴⁷



334

335 **Figure 5.** (a) Percent of the global population exposed to 10 ppb intervals of OSDMA8 from
 336 1990-2017. (b) Ozone trend regionally (regions defined in Figure S1) over 1990–2017 for the
 337 metric of population weighted OSDMA8. All trends have p-values less than 0.05, except for
 338 Europe and South America (Table S3). Uncertainty intervals are included in Figures S33-46.

339 **DISCUSSION**

340 We create fine resolution yearly ozone distributions for 1990–2017 that incorporate
341 surface observations and output from nine atmospheric chemistry models, using a novel
342 combination of the M³Fusion method for creating a multi-model composite, which dominates the
343 large-scale ozone estimates, and BME data fusion which influences ozone estimates near
344 observation locations, smoothly integrating observations in space and time. Our analysis finds
345 that methods incorporating observations outperform ozone estimated from models only.
346 Additionally, the influence of an observation across multiple years in BME further improves our
347 ozone estimate. Our method’s major strengths include the incorporation of multiple data types,
348 the smooth weighting of observational influence across space and time, the ability to output a
349 variance at every estimation point, and the estimation of global ozone with fine spatial structure.
350 The improvement in model performance from using our combination of M³Fusion and BME
351 provides a caution against using simple spatial interpolations of observations or output of a
352 model without bias correction, to represent ozone. Although we improve upon the previous
353 GBD ozone estimate, some limitations remain. The lack of monitoring stations in large populous
354 regions limits our abilities to understand ozone exposure in these areas, where these uncertainties
355 affect both the multi-model composite and BME data fusion. Our method is limited in years with
356 fewer observations and models available; additionally, the fine resolution model output that
357 informs the fine spatial pattern of our output is only available for a single year. Future work may
358 apply a nonlinear bias correction, or use machine learning to correct bias,⁶⁰ to the multi-model
359 composite to improve the global offset, and thus the overall estimation. Our work also shows the
360 value of using multiple models in creating a multi-model composite, as output from each model
361 was selected (weight>0) in at least some regions and years.

362 Our method can be applied to future years as more observations and model output
363 become available. Additionally, our method can be used to estimate ozone metrics other than
364 OSDMA8, including for studies of vegetation and crop impacts.⁶¹ While model output and
365 geostatistical techniques like BME can estimate global ozone, estimates suffer from the lack of
366 observations in some world regions. Additional observations, especially in unmonitored regions
367 with large populations including megacities in low- and middle-income nations, are essential to
368 improve understanding of ozone exposure and health burden.

369 Ozone exposure is increasing globally, with global population-weighted ozone showing a
370 positive trend from 1990-2017, driven by strong positive trends in highly populated and polluted
371 regions of Asia and Africa. The increasing global exposure to ozone indicates that current ozone
372 management policies are failing to reduce ozone exposure in many regions of the world. Our
373 results can be used by policy makers to identify regions where ozone pollution could be
374 mitigated through reductions of ozone precursor emissions, mainly from fossil-fuel combustion,
375 on local, national and continental scales, or through international agreements to reduce
376 emissions, including methane, that affect global background ozone.^{62,63}

377 **ASSOCIATED CONTENT**

378 **Supporting Information.** The supporting information includes multi-model composite model
379 weights, covariance parameters, fine resolution addition example, yearly maps for all relevant
380 scenarios, cross validation statistics, and national ozone trends with uncertainty intervals.

381 **AUTHOR INFORMATION**

382 Corresponding Author: J. Jason West, jasonwest@unc.edu, 919-843-3928.

383 **ACKNOWLEDGEMENTS**

384 We acknowledge support from the NASA Health and Air Quality Applied Sciences Team
385 (#NNX16AQ30G) and the National Institute for Occupational Safety and Health (T42-
386 OH008673). Makoto Deushi was supported by the Japan Society for the Promotion of Science
387 (JP20K04070).

388

389 REFERENCES

- 390 (1) Jerrett, M.; Burnett, R. T.; Arden Pope, C.; Ito, K.; Thurston, G.; Krewski, D.; Shi, Y.;
391 Calle, E.; Thun, M. Long-Term Ozone Exposure and Mortality. *N. Engl. J. Med.* **2009**,
392 *360* (11), 1085–1095. <https://doi.org/10.1056/NEJMoa0803894>.
- 393 (2) Turner, M. C.; Jerrett, M.; Pope, C. A.; Krewski, D.; Gapstur, S. M.; Diver, W. R.;
394 Beckerman, B. S.; Marshall, J. D.; Su, J.; Crouse, D. L.; Burnett, R. T. Long-Term Ozone
395 Exposure and Mortality in a Large Prospective Study. *Am. J. Respir. Crit. Care Med.*
396 **2016**, *193* (10), 1134–1142. <https://doi.org/10.1164/rccm.201508-1633OC>.
- 397 (3) Di, Q.; Dai, L.; Wang, Y.; Zanobetti, A.; Choirat, C.; Schwartz, J. D.; Dominici, F.
398 Association of short-term exposure to air pollution with mortality in older adults, *J. Amer.*
399 *Med. Assoc.* **2017**, *318* (24), 2446-2456. doi: 10.1001/jama.2017.17923.(4) Myhre, G.,
400 Shindell, D., Bréon, F.-M., Collins, W., Fuglestedt, J., Huang, J., Koch, D., Lamarque,
401 J.-F., Lee, D., Mendoza, B., et al. Anthropogenic and Natural Radiative Forcing. In:
402 Climate Change 2013: The Physical Science Basis. Contribution of Working Group I to
403 the Fifth Assessment Report of the Intergovernmental Panel on Climate Change [Stocker,
404 T.F., D. Qin, G.-K. Plattner, M. Ti; Cambridge University Press: Cambridge, United
405 Kingdom and New York, NY, USA, 2013.
- 406 (5) U.S. EPA. *Integrated Science Assessment for Ozone and Related Photochemical*

407 *Oxidants*; U.S. Environmental Protection Agency, Washington, DC, EPA/600/R-20/012,
408 2020.

409 (6) Emberson, L. D.; Pleijel, H.; Ainsworth, E. A.; van den Berg, M.; Ren, W.; Osborne, S.;
410 Mills, G.; Pandey, D.; Dentener, F.; B ker, P.; et al. Ozone Effects on Crops and
411 Consideration in Crop Models. *Eur. J. Agron.* **2018**, *100*, 19–34.
412 <https://doi.org/10.1016/j.eja.2018.06.002>.

413 (7) Fleming, Z. L.; Doherty, R. M.; Von Schneidmesser, E.; Malley, C. S.; Cooper, O. R.;
414 Pinto, J. P.; Colette, A.; Xu, X.; Simpson, D.; Schultz, M. G.; et al. Tropospheric Ozone
415 Assessment Report: Present-Day Ozone Distribution and Trends Relevant to Human
416 Health. *Elementa* **2018**, *6* (1). <https://doi.org/10.1525/elementa.273>.

417 (8) Cooper, O. R.; Parrish, D. D.; Ziemke, J.; Balashov, N. V.; Cupeiro, M.; Galbally, I. E.;
418 Gilge, S.; Horowitz, L.; Jensen, N. R.; Lamarque, J.-F.; et al. Global Distribution and
419 Trends of Tropospheric Ozone: An Observation-Based Review. *Elem. Sci. Anthr.* **2014**, *2*
420 (0), 000029. <https://doi.org/10.12952/journal.elementa.000029>.

421 (9) Lim, S. S.; Vos, T.; Flaxman, A. D.; Danaei, G.; Shibuya, K.; Adair-Rohani, H.; Amann,
422 M.; Anderson, H. R.; Andrews, K. G.; Aryee, M.; et al. A Comparative Risk Assessment
423 of Burden of Disease and Injury Attributable to 67 Risk Factors and Risk Factor Clusters
424 in 21 Regions, 1990-2010: A Systematic Analysis for the Global Burden of Disease Study
425 2010. *Lancet* **2012**, *380* (9859), 2224–2260. [https://doi.org/10.1016/S0140-](https://doi.org/10.1016/S0140-6736(12)61766-8)
426 [6736\(12\)61766-8](https://doi.org/10.1016/S0140-6736(12)61766-8).

427 (10) Cohen, A. J.; Brauer, M.; Burnett, R.; Anderson, H. R.; Frostad, J.; Estep, K.;
428 Balakrishnan, K.; Brunekreef, B.; Dandona, L.; Dandona, R.; et al. Estimates and 25-Year
429 Trends of the Global Burden of Disease Attributable to Ambient Air Pollution: An

430 Analysis of Data from the Global Burden of Diseases Study 2015. *Lancet* **2017**, 389
431 (10082), 1907–1918. [https://doi.org/10.1016/S0140-6736\(17\)30505-6](https://doi.org/10.1016/S0140-6736(17)30505-6).

432 (11) Shaddick, G.; Thomas, M. L.; Green, A.; Brauer, M.; van Donkelaar, A.; Burnett, R.;
433 Chang, H. H.; Cohen, A.; Dingenen, R. Van; Dora, C.; et al. Data Integration Model for
434 Air Quality: A Hierarchical Approach to the Global Estimation of Exposures to Ambient
435 Air Pollution. *J. R. Stat. Soc. Ser. C Appl. Stat.* **2018**, 67 (1), 231–253.
436 <https://doi.org/10.1111/rssc.12227>.

437 (12) Shaddick, G.; Thomas, M. L.; Amini, H.; Broday, D.; Cohen, A.; Frostad, J.; Green, A.;
438 Gumy, S.; Liu, Y.; Martin, R. V.; et al. Data Integration for the Assessment of Population
439 Exposure to Ambient Air Pollution for Global Burden of Disease Assessment. *Environ.*
440 *Sci. Technol.* **2018**, 52 (16), 9069–9078. <https://doi.org/10.1021/acs.est.8b02864>.

441 (13) Stanaway, J. D.; Afshin, A.; Gakidou, E.; Lim, S. S.; Abate, D.; Abate, K. H.; Abbafati,
442 C.; Abbasi, N.; Abbastabar, H.; Abd-Allah, F.; et al. Global, Regional, and National
443 Comparative Risk Assessment of 84 Behavioural, Environmental and Occupational, and
444 Metabolic Risks or Clusters of Risks for 195 Countries and Territories, 1990–2017: A
445 Systematic Analysis for the Global Burden of Disease Study 2017. *Lancet* **2018**, 392
446 (10159), 1923–1994. [https://doi.org/10.1016/S0140-6736\(18\)32225-6](https://doi.org/10.1016/S0140-6736(18)32225-6).

447 (14) Brauer, M.; Freedman, G.; Frostad, J.; Van Donkelaar, A.; Martin, R. V.; Dentener, F.;
448 Dingenen, R. Van; Estep, K.; Amini, H.; Apte, J. S.; et al. Ambient Air Pollution
449 Exposure Estimation for the Global Burden of Disease 2013. *Environ. Sci. Technol.* **2016**,
450 50 (1), 79–88. <https://doi.org/10.1021/acs.est.5b03709>.

451 (15) Gaudel, A.; Cooper, O. R.; Ancellet, G.; Barret, B.; Boynard, A.; Burrows, J. P.;
452 Clerbaux, C.; Coheur, P. F.; Cuesta, J.; Cuevas, E.; et al. Tropospheric Ozone Assessment

- 453 Report: Present-Day Distribution and Trends of Tropospheric Ozone Relevant to Climate
454 and Global Atmospheric Chemistry Model Evaluation. *Elementa* **2018**, 6 (1).
455 <https://doi.org/10.1525/elementa.291>.
- 456 (16) Schultz, M. G.; Schröder, S.; Lyapina, O.; Cooper, O.; Galbally, I.; Petropavlovskikh, I.;
457 Von Schneidemesser, E.; Tanimoto, H.; Elshorbany, Y.; Naja, M.; et al. Tropospheric
458 Ozone Assessment Report: Database and Metrics Data of Global Surface Ozone
459 Observations. *Elem Sci Anth* **2017**, 5 (0), 58. <https://doi.org/10.1525/elementa.244>.
- 460 (17) Morgenstern, O.; Hegglin, M.; Rozanov, E.; O'Connor, F.; Luke Abraham, N.; Akiyoshi,
461 H.; Archibald, A.; Bekki, S.; Butchart, N.; Chipperfield, M.; et al. Review of the Global
462 Models Used within Phase 1 of the Chemistry-Climate Model Initiative (CCMI).
463 *Geoscientific Model Development*. Copernicus GmbH February 13, 2017, pp 639–671.
464 <https://doi.org/10.5194/gmd-10-639-2017>.
- 465 (18) Chang, K.-L.; Cooper, O. R.; West, J. J.; Serre, M. L.; Schultz, M. G.; Lin, M.; Marécal,
466 V.; Josse, B.; Deushi, M.; Sudo, K.; et al. A New Method (M³ Fusion v1) for Combining
467 Observations and Multiple Model Output for an Improved Estimate of the Global Surface
468 Ozone Distribution. *Geosci. Model Dev.* **2019**, 12 (3), 955–978.
469 <https://doi.org/10.5194/gmd-12-955-2019>.
- 470 (19) Christakos, G. A Bayesian/Maximum-Entropy View to the Spatial Estimation Problem.
471 *Math. Geol.* **1990**, 22 (7), 763–777. <https://doi.org/10.1007/BF00890661>.
- 472 (20) Christakos, G.; Bogaert, P.; Serre, M. L. *Temporal GIS: Advanced Functions for Field-*
473 *Based Applications*; Springer Berlin Heidelberg, 2001.
- 474 (21) Serre, M. L.; Christakos, G. Modern Geostatistics: Computational BME Analysis in the
475 Light of Uncertain Physical Knowledge - The Equus Beds Study. *Stoch. Environ. Res.*

- 476 *Risk Assess.* **1999**, *13* (1–2), 1–26. <https://doi.org/10.1007/s004770050029>.
- 477 (22) Christakos, G.; Kolovos, A.; Serre, M. L.; Vukovich, F. Total Ozone Mapping by
478 Integrating Databases from Remote Sensing Instruments and Empirical Models. *IEEE*
479 *Trans. Geosci. Remote Sens.* **2004**, *42* (5), 991–1008.
480 <https://doi.org/10.1109/TGRS.2003.822751>.
- 481 (23) Nazelle, A. De; Arunachalam, S.; Serre, M. L. Bayesian Maximum Entropy Integration of
482 Ozone Observations and Model Predictions: An Application for Attainment
483 Demonstration in North Carolina. *Environ. Sci. Technol.* **2010**, *44* (15), 5707–5713.
484 <https://doi.org/10.1021/es100228w>.
- 485 (24) Xu, Y.; Serre, M. L.; Reyes, J.; Vizuete, W. Bayesian Maximum Entropy Integration of
486 Ozone Observations and Model Predictions: A National Application. *Environ. Sci.*
487 *Technol.* **2016**, *50* (8), 4393–4400. <https://doi.org/10.1021/acs.est.6b00096>.
- 488 (25) Xu, Y.; Serre, M. L.; Reyes, J. M.; Vizuete, W. Impact of Temporal Upscaling and
489 Chemical Transport Model Horizontal Resolution on Reducing Ozone Exposure
490 Misclassification. *Atmos. Environ.* **2017**, *166*, 374–382.
491 <https://doi.org/10.1016/j.atmosenv.2017.07.033>.
- 492 (26) Hu, L.; Keller, C. A.; Long, M. S.; Sherwen, T.; Auer, B.; Da Silva, A.; Nielsen, J. E.;
493 Pawson, S.; Thompson, M. A.; Trayanov, A. L.; et al. Global Simulation of Tropospheric
494 Chemistry at 12.5&Thinsp;Km Resolution: Performance and Evaluation of the
495 GEOS-Chem Chemical Module (V10-1) within the NASA GEOS Earth System Model
496 (GEOS-5 ESM). *Geosci. Model Dev.* **2018**, *11* (11), 4603–4620.
497 <https://doi.org/10.5194/gmd-11-4603-2018>.
- 498 (27) Murray, C. J. L.; Aravkin, A. Y.; Zheng, P.; Abbafati, C.; Abbas, K. M.; Abbasi-

499 Kangevari, M.; Abd-Allah, F.; Abdelalim, A.; Abdollahi, M.; Abdollahpour, I.; et al.
500 Global Burden of 87 Risk Factors in 204 Countries and Territories, 1990–2019: A
501 Systematic Analysis for the Global Burden of Disease Study 2019. *Lancet* **2020**, *396*
502 (10258), 1223–1249. [\(28\)](https://doi.org/10.1016/S0140-6736(20)30752-2) Seltzer, K. M.;
503 Shindell, D. T.; Kasibhatla, P.; Malley, C. S. Magnitude, Trends, and Impacts of Ambient
504 Long-Term Ozone Exposure in the United States from 2000 to 2015. *Atmos. Chem. Phys.*
505 **2020**, *20* (3), 1757–1775. <https://doi.org/10.5194/acp-20-1757-2020>.

506 (29) Kleinert, F.; Leufen, L.; Schultz, M. IntelliO3-Ts v1.0: A Neural Network Approach to
507 Predict near-Surface Ozone Concentrations in Germany. *Geosci. Model Dev. Discuss.*
508 **2020**, 1–69. <https://doi.org/10.5194/gmd-2020-169>.

509 (30) Schultz, Martin G; Schröder, Sabine; Lyapina, Olga; Cooper, Owen R; Galbally, Ian;
510 Petropavlovskikh, Irina; von Schneidemesser, Erika; Tanimoto, Hiroshi; Elshorbany,
511 Yasin; Naja, Manish; et al. Tropospheric Ozone Assessment Report, Links to Global
512 Surface Ozone Datasets. *PANGAEA* **2017**.

513 (31) Lu, X.; Hong, J.; Zhang, L.; Cooper, O. R.; Schultz, M. G.; Xu, X.; Wang, T.; Gao, M.;
514 Zhao, Y.; Zhang, Y. Severe Surface Ozone Pollution in China: A Global Perspective.
515 *Environ. Sci. Technol. Lett.* **2018**, *5* (8), 487–494.
516 <https://doi.org/10.1021/acs.estlett.8b00366>.

517 (32) Orbe, C.; Plummer, D. A.; Waugh, D. W.; Yang, H.; Jöckel, P.; Kinnison, D. E.; Josse, B.;
518 Marecal, V.; Deushi, M.; Abraham, N. L.; et al. Description and Evaluation of the
519 Specified-Dynamics Experiment in the Chemistry-Climate Model Initiative. *Atmos. Chem.*
520 *Phys.* **2020**, *20* (6), 3809–3840. <https://doi.org/10.5194/acp-20-3809-2020>.

521 (33) Lamarque, J.-F.; Bond, T. C.; Eyring, V.; Granier, C.; Heil, A.; Klimont, Z.; Lee, D.;

522 Lioussé, C.; Mieville, A.; Owen, B.; et al. Historical (1850–2000) Gridded Anthropogenic
523 and Biomass Burning Emissions of Reactive Gases and Aerosols: Methodology and
524 Application. *Atmos. Chem. Phys.* **2010**, *10* (15), 7017–7039. [https://doi.org/10.5194/acp-](https://doi.org/10.5194/acp-10-7017-2010)
525 [10-7017-2010](https://doi.org/10.5194/acp-10-7017-2010).

526 (34) Granier, C.; Bessagnet, B.; Bond, T.; D’Angiola, A.; van der Gon, H. D.; Frost, G. J.;
527 Heil, A.; Kaiser, J. W.; Kinne, S.; Klimont, Z.; et al. Evolution of Anthropogenic and
528 Biomass Burning Emissions of Air Pollutants at Global and Regional Scales during the
529 1980-2010 Period. *Clim. Change* **2011**, *109* (1), 163–190. [https://doi.org/10.1007/s10584-](https://doi.org/10.1007/s10584-011-0154-1)
530 [011-0154-1](https://doi.org/10.1007/s10584-011-0154-1).

531 (35) Eyring, V.; Bony, S.; Meehl, G. A.; Senior, C. A.; Stevens, B.; Stouffer, R. J.; Taylor, K.
532 E. Overview of the Coupled Model Intercomparison Project Phase 6 (CMIP6)
533 Experimental Design and Organization. *Geosci. Model Dev.* **2016**, *9* (5), 1937–1958.
534 <https://doi.org/10.5194/gmd-9-1937-2016>.

535 (36) Tilmes, S.; Lamarque, J.-F.; Emmons, L. K.; Kinnison, D. E.; Ma, P.-L.; Liu, X.; Ghan,
536 S.; Bardeen, C.; Arnold, S.; Deeter, M.; et al. Description and Evaluation of Tropospheric
537 Chemistry and Aerosols in the Community Earth System Model (CESM1.2). *Geosci.*
538 *Model Dev.* **2015**, *8* (5), 1395–1426. <https://doi.org/10.5194/gmd-8-1395-2015>.

539 (37) Garcia, R. R.; Smith, A. K.; Kinnison, D. E.; de la Cámara, Á.; Murphy, D. J.
540 Modification of the Gravity Wave Parameterization in the Whole Atmosphere Community
541 Climate Model: Motivation and Results. *J. Atmos. Sci.* **2017**, *74* (1), 275–291.
542 <https://doi.org/10.1175/JAS-D-16-0104.1>.

543 (38) Marsh, D. R.; Mills, M. J.; Kinnison, D. E.; Lamarque, J. F.; Calvo, N.; Polvani, L. M.
544 Climate Change from 1850 to 2005 Simulated in CESM1(WACCM). *J. Clim.* **2013**, *26*

- 545 (19), 7372–7391. <https://doi.org/10.1175/JCLI-D-12-00558.1>.
- 546 (39) Sudo, K.; Takahashi, M.; Kurokawa, J.; Akimoto, H. CHASER: A Global Chemical
547 Model of the Troposphere 1. Model Description. *J. Geophys. Res. Atmos.* **2002**, *107*
548 (D17), ACH 7-1-ACH 7-20. <https://doi.org/10.1029/2001JD001113>.
- 549 (40) Sudo, K.; Takahashi, M.; Akimoto, H. CHASER: A Global Chemical Model of the
550 Troposphere 2. Model Results and Evaluation. *J. Geophys. Res. Atmos.* **2002**, *107* (D21),
551 ACH 9-1-ACH 9-39. <https://doi.org/10.1029/2001JD001114>.
- 552 (41) Watanabe, S.; Hajima, T.; Sudo, K.; Nagashima, T.; Takemura, T.; Okajima, H.; Nozawa,
553 T.; Kawase, H.; Abe, M.; Yokohata, T.; et al. MIROC-ESM 2010: Model Description and
554 Basic Results of CMIP5-20c3m Experiments. *Geosci. Model Dev.* **2011**, *4* (4), 845–872.
555 <https://doi.org/10.5194/gmd-4-845-2011>.
- 556 (42) Lin, M.; Fiore, A. M.; Horowitz, L. W.; Cooper, O. R.; Naik, V.; Holloway, J.; Johnson,
557 B. J.; Middlebrook, A. M.; Oltmans, S. J.; Pollack, I. B.; et al. Transport of Asian Ozone
558 Pollution into Surface Air over the Western United States in Spring. *J. Geophys. Res.*
559 *Atmos.* **2012**, *117* (4). <https://doi.org/10.1029/2011JD016961>.
- 560 (43) Lin, M.; Horowitz, L. W.; Oltmans, S. J.; Fiore, A. M.; Fan, S. Tropospheric Ozone
561 Trends at Mauna Loa Observatory Tied to Decadal Climate Variability. *Nat. Geosci.*
562 **2014**, *7* (2), 136–143. <https://doi.org/10.1038/ngeo2066>.
- 563 (44) Lin, M.; Horowitz, L. W.; Payton, R.; Fiore, A. M.; Tonnesen, G. US Surface Ozone
564 Trends and Extremes from 1980 to 2014: Quantifying the Roles of Rising Asian
565 Emissions, Domestic Controls, Wildfires, and Climate. *Atmos. Chem. Phys.* **2017**, *17* (4),
566 2943–2970. <https://doi.org/10.5194/acp-17-2943-2017>.
- 567 (45) Zhang, L.; Lin, M.; Langford, A.; Horowitz, L.; Senff, C.; Klovenski, E.; Wang, Y.;

568 Alvarez II, R.; Petropavlovskikh, I.; Cullis, P.; et al. Characterizing Sources of High
569 Surface Ozone Events in the Southwestern U.S. with Intensive Field Measurements and
570 Two Global Models. *Atmos. Chem. Phys.* **2019**, 1–47. [https://doi.org/10.5194/acp-2019-](https://doi.org/10.5194/acp-2019-990)
571 990.

572 (46) Horowitz, L. W., Naik, V., Paulot, F., Ginoux, P., Dunne, J. P., Mao, J. Q., et al. The
573 GFDL Global Atmospheric Chemistry-Climate Model AM4.1: Model Description and
574 Simulation Characteristics. *J. Adv. Model. Earth Syst.* **2020**, *submitted*.

575 (47) Ziemke, J. R.; Oman, L. D.; Strode, S. A.; Douglass, A. R.; Olsen, M. A.; McPeters, R.
576 D.; Bhartia, P. K.; Froidevaux, L.; Labow, G. J.; Witte, J. C.; et al. Trends in Global
577 Tropospheric Ozone Inferred from a Composite Record of TOMS/OMI/MLS/OMPS
578 Satellite Measurements and the MERRA-2 GMI Simulation. *Atmos. Chem. Phys.* **2019**, *19*
579 (5), 3257–3269. <https://doi.org/10.5194/acp-19-3257-2019>.

580 (48) Strode, S. A.; Ziemke, J. R.; Oman, L. D.; Lamsal, L. N.; Olsen, M. A.; Liu, J. Global
581 Changes in the Diurnal Cycle of Surface Ozone. *Atmos. Environ.* **2019**, *199*, 323–333.
582 <https://doi.org/10.1016/j.atmosenv.2018.11.028>.

583 (49) Josse, B.; Simon, P.; Peuch, V.-H. Radon Global Simulations with the Multiscale
584 Chemistry and Transport Model MOCAGE. *Tellus B Chem. Phys. Meteorol.* **2004**, *56* (4),
585 339–356. <https://doi.org/10.3402/tellusb.v56i4.16448>.

586 (50) Teyssède, H.; Michou, M.; Clark, H. L.; Josse, B.; Karcher, F.; Olivie, D.; Peuch, V.-H.;
587 Saint-Martin, D.; Cariolle, D.; Attié, J.-L.; et al. New Tropospheric and Stratospheric
588 Chemistry and Transport Model MOCAGE-Climat for Multi-Year Studies: Evaluation of
589 the Present-Day Climatology and Sensitivity to Surface Processes. *Atmos. Chem. Phys.*
590 **2007**, *7* (22), 5815–5860. <https://doi.org/10.5194/acp-7-5815-2007>.

- 591 (51) Adachi, Y.; Yukimoto, S.; Deushi, M.; Obata, A.; Nakano, H.; Tanaka, T. Y.; Hosaka, M.;
592 Sakami, T.; Yoshimura, H.; Hirabara, M.; et al. Basic Performance of a New Earth System
593 Model of the Meteorological Research Institute. *Pap. Meteorol. Geophys.* **2013**, *64*, 1–19.
594 <https://doi.org/10.2467/mripapers.64.1>.
- 595 (52) Yukimoto, S.; Kawai, H.; Koshiro, T.; Oshima, N.; Yoshida, K.; Urakawa, S.; Tsujino, H.;
596 Deushi, M.; Tanaka, T.; Hosaka, M.; et al. The Meteorological Research Institute Earth
597 System Model Version 2.0, MRI-ESM2.0: Description and Basic Evaluation of the
598 Physical Component. *J. Meteorol. Soc. Japan* **2019**, *97* (5), 931–965.
599 <https://doi.org/10.2151/jmsj.2019-051>.
- 600 (53) Bolin, D.; Lindgren, F. Spatial Models Generated by Nested Stochastic Partial Differential
601 Equations, with an Application to Global Ozone Mapping. *Ann. Appl. Stat.* **2011**, *5* (1),
602 523–550. <https://doi.org/10.1214/10-AOAS383>.
- 603 (54) Christakos, G. *Modern Spatiotemporal Geostatistics*; Oxford University Press: Cary, NC,
604 2000.
- 605 (55) Freire, L. S.; Gerken, T.; Ruiz-Plancarte, J.; Wei, D.; Fuentes, J. D.; Katul, G. G.; Dias, N.
606 L.; Acevedo, O. C.; Chamecki, M. Turbulent Mixing and Removal of Ozone within an
607 Amazon Rainforest Canopy. *J. Geophys. Res. Atmos.* **2017**, *122* (5), 2791–2811.
608 <https://doi.org/10.1002/2016JD026009>.
- 609 (56) Bauer, S. E.; Im, U.; Mezuman, K.; Gao, C. Y. Desert Dust, Industrialization, and
610 Agricultural Fires: Health Impacts of Outdoor Air Pollution in Africa. *J. Geophys. Res.*
611 *Atmos.* **2019**, *124* (7), 4104–4120. <https://doi.org/10.1029/2018JD029336>.
- 612 (57) Chang, K.-L.; Petropavlovskikh, I.; Copper, O. R.; Schultz, M. G.; Wang, T. Regional
613 Trend Analysis of Surface Ozone Observations from Monitoring Networks in Eastern

614 North America, Europe and East Asia. *Elem Sci Anth* **2017**, 5 (0), 50.
615 <https://doi.org/10.1525/elementa.243>.

616 (58) Li, K.; Jacob, D. J.; Liao, H.; Shen, L.; Zhang, Q.; Bates, K. H. Anthropogenic Drivers of
617 2013–2017 Trends in Summer Surface Ozone in China. *Proc. Natl. Acad. Sci. U. S. A.*
618 **2019**, 116 (2), 422–427. <https://doi.org/10.1073/pnas.1812168116>.

619 (59) Gaudel, A.; Cooper, O. R.; Chang, K. L.; Bourgeois, I.; Ziemke, J. R.; Strode, S. A.;
620 Oman, L. D.; Sellitto, P.; Nédélec, P.; Blot, R.; et al. Aircraft Observations since the
621 1990s Reveal Increases of Tropospheric Ozone at Multiple Locations across the Northern
622 Hemisphere. *Sci. Adv.* **2020**, 6 (34). <https://doi.org/10.1126/sciadv.aba8272>.

623 (60) Ivatt, P. D.; Evans, M. J. Improving the Prediction of an Atmospheric Chemistry
624 Transport Model Using Gradient-Boosted Regression Trees. *Atmos. Chem. Phys.* **2020**, 20
625 (13), 8063–8082. <https://doi.org/10.5194/acp-20-8063-2020>.

626 (61) Mills, G.; Pleijel, H.; Malley, C. S.; Sinha, B.; Cooper, O. R.; Schultz, M. G.; Neufeld, H.
627 S.; Simpson, D.; Sharps, K.; Feng, Z.; et al. Tropospheric Ozone Assessment Report:
628 Present-Day Tropospheric Ozone Distribution and Trends Relevant to Vegetation.
629 *Elementa* **2018**, 6 (1). <https://doi.org/10.1525/elementa.302>.

630 (62) West, J. J.; Fiore, A. M.; Horowitz, L. W.; Mauzerall, D. L. Global Health Benefits of
631 Mitigating Ozone Pollution with Methane Emission Controls. *Proc. Natl. Acad. Sci. U. S.*
632 *A.* **2006**, 103 (11), 3988–3993. <https://doi.org/10.1073/pnas.0600201103>.

633 (63) Dentener, F.; Keating, T.; Akimoto, H. *Hemispheric Transport of Air Pollution: Part A:*
634 *Ozone and Particulate Matter*; Economic Commission for Europe, Geneva, 2010.

635